Journal of Marine Research, 55, 181–200, 1997

Journal of
MARINE RESEARCH

Volume 55, Number 2

Eddy formation on a continental slope

by Janet M. Becker[1] and Rick Salmon[2]

ABSTRACT

We consider a uniform-density ocean in which the depth-independent horizontal velocity is driven by a two-gyre wind. Numerical solutions of the governing vorticity equation reveal that the solutions with a flat ocean bottom differ greatly from those in which a continental shelf and slope are present along the western boundary. In the ocean basin with a western continental shelf, steady inertial circulations readily lose stability to unsteady inertial circulations that spawn eddies. However, eddies do not form in the corresponding solutions for the flat-bottom ocean. Reducing the friction leads to flat-bottom solutions that shed eddies far offshore, but still differ significantly from the corresponding continental-slope solutions, where eddies pinch off near the western boundary.

1. Introduction

Our physical understanding of western boundary currents rests upon simple dynamical models. The first (and still perhaps most influential) such models were those of Stommel (1948) and Munk (1950), who neglected the inertia of the fluid, and considered the vertically integrated flow in a rectangular ocean with a flat bottom (and, hence, vertical sidewalls). In the flat-bottom, inertia-less models of Stommel and Munk, the western boundary current occupies a frictional boundary layer at the coast.

The two assumptions of a flat ocean bottom and negligible inertia are of course unrealistic, particularly near western boundary currents, where observations show that the flow is strong and extends almost undiminished to the relatively steeply sloping ocean bottom. However, the relaxation of *either* assumption couples the equation for the vertically integrated flow to the baroclinic (i.e. depth-dependent) motion, raising the

1. Department of Ocean Engineering, University of Hawaii at Manoa, 2540 Dole Street, Holmes Hall 402, Honolulu, Hawaii, 96822, U.S.A.
2. Scripps Institution of Oceanography, La Jolla, California, 92093-0225, U.S.A.

complexity of the problem to a level no longer amenable to simple analysis or easy numerical solution. For this reason, theorists trying to explain the role of inertia in western boundary currents have often considered the case of *homogeneous* fluid, and assumed *a priori* that the horizontal velocity is independent of depth. In the case of homogeneous, depth-independent flow, the governing dynamical equation remains a single, two-dimensional equation in the stream function $\psi(x, y, t)$ for the vertically-integrated horizontal transport. Although nonlinear, this equation is still somewhat tractable to a combination of numerical and analytical methods. Curiously, however, most studies of nonlinear, depth-independent motion have continued to consider the case of a flat ocean bottom. This is somewhat surprising, because once the assumption of depth-independent flow has been made, the governing ψ-equation is really no more complicated with bottom topography than without it.

In this paper, we present numerical solutions of the equation (2.9–10) governing homogeneous, depth-independent flow, driven by a two-gyre wind, in a rectangular ocean of depth $H(x, y)$. To demonstrate the importance of the western continental slope, we compare solutions in which H vanishes smoothly at the western boundary to the corresponding solutions with a flat ocean bottom. We find that the flow is completely different in the two cases and (we believe) much more realistic in the case where a smooth continental slope replaces the vertical wall at the western boundary.

In both cases, the lines of constant f/H (where f is the Coriolis parameter) represent *characteristic lines* in the limit of vanishing nonlinearity and dissipation (in which the steady ψ-equation becomes hyperbolic). In the case of a flat bottom, these characteristic lines intersect the western boundary, leading to the formation of a frictional or inertial boundary layer at the vertical sidewall. However, in the case of a western continental slope, the topography bends the characteristic lines nearly parallel to the coastline, and boundary layers are not required. In the (linear) limit of weak wind-forcing, the western boundary currents on the continental slope flow along characteristic lines at some distance from the coastline, and are completely controlled by the topography; friction is almost everywhere unimportant.

In both cases, inertia becomes important near the western boundary as the winds become realistically strong. However, in the case where a western continental slope is present, steady inertial solutions lose their stability much more readily, and eddies form within the boundary current itself. We do not observe such significant eddy formation in the corresponding solutions with a flat bottom.

Although our results are primarily descriptive, we offer a physical interpretation based upon the interaction between vortex layers already present in the (linear) limit of weak wind-forcing. In the linear limit, and for the case of a flat bottom, these vortex layers lie within the frictional western boundary layer and are well separated from one another (Fig. 2b). As the wind strength increases, the vortex layers are advected by the flow (Fig. 3b), but do not interact significantly until advection has pulled the vortex layers far

offshore into a nearly parallel configuration. Even then, eddies form far offshore at the eastern end of the vortex layers only if the friction is relatively weak (Fig. 11).

In contrast, in the case of a western continental slope, the vortex layers are already nearly parallel in the linear limit (Fig. 2d), and therefore strongly interact as the wind-forcing (and nonlinearity) increase (Fig. 3d). Eddies form readily (Fig. 6), as the stronger vortex sheet wraps the weaker sheet around its tip.

The literature on the flat-bottom case is long-running and extensive. Veronis (1966) determined the effects of increasing the Rossby number on the solutions of the wind-driven vorticity equation with bottom friction for which the zero Rossby number solution is Stommel's circulation. He found a sequence of steady solutions that lead, in the limit of large Rossby number, to a steady solution resembling that of Fofonoff (1954). In contrast, Bryan (1963) found that, with lateral diffusion, Munk's zero-Rossby-number solution loses stability to unsteady solutions as the Rossby number is increased. Hendershott (1987) reviews the literature on single-layer circulation models through the mid-1980's. Recently, Ierley and Sheremet (1995) and Cessi and Ierley (1995) have discovered multiple steady solutions of the wind-driven vorticity equation in a flat-bottom ocean for a fixed set of control parameters and have analyzed these with bifurcation theory. Meacham and Berloff (1997) have explored the transition to multiple unsteady solutions of the wind-driven vorticity equation in a flat-bottom ocean. This work is part of a promising effort to understand the types of solutions that may occur in more realistic models of the general circulation.

In contrast, there have been relatively few studies of homogeneous flow in basins with sloping boundaries. Holland (1967) solved the steady, wind-driven vorticity equation with inertia and lateral diffusion in a basin for which a continental shelf separates a shallow coastal region from the deep ocean and noted the importance of isopleths of constant f/H in determining the model circulations. Welander (1968) exploited the analogy between a thermal advection-diffusion equation and the linear, steady vorticity equation with a bottom Ekman layer and showed how the boundary current structure is affected by the sign of the meridional derivative of f/H. Recently, Nishigaki (1995) modeled a steady, inviscid, inertial boundary current over a continental slope as the boundary between an inshore stagnant region and an offshore gyre across which the pressure is continuous. These studies, however, have been limited to steady circulations in basins in which the shelf is bounded by a vertical coastal sidewall.

Of course, homogeneous-fluid models exaggerate the importance of ocean bottom topography. In the real ocean, the strongest mean currents and their accompanying horizontal pressure gradients occur in the main thermocline, and hence induce a much smaller bottom torque than if uniformly distributed with depth. However, this thermocline region *intersects* the ocean bottom along western continental slopes, and the resulting *large* bottom torque directs the flow along isobaths at some distance from the shoreline. Thus our model, which is homogeneous, but includes the western continental slope as the *only* topography present, may represent a sensible compromise between simplicity and realism.

In any case, we feel that it is a much better paradigm than the more traditional models with a flat ocean bottom, in which vorticity advection competes not with bottom torque, but with the torque arising from the rather artificial eddy friction. In flat-bottom models, this frictional torque assumes an exaggerated importance, because the more realistic bottom torque is absent.

2. Dynamics and numerical method

We consider homogeneous (i.e. uniform-density) fluid governed by the (hydrostatic) primitive equations,

$$\frac{D\mathbf{u}}{Dt} + f\mathbf{k} \times \mathbf{u} = -\nabla\phi - R\mathbf{u} + \frac{\tau_s - \tau_b}{H}, \tag{2.1}$$

$$0 = -\frac{\partial\phi}{\partial z} \tag{2.2}$$

$$\nabla \cdot \mathbf{u} + \frac{\partial w}{\partial z} = 0. \tag{2.3}$$

Here, $\mathbf{u}$ is the horizontal part of the velocity $(\mathbf{u}, w)$, $f = \beta y$ is the Coriolis parameter, $\mathbf{k}$ is the vertical unit vector, $\nabla = (\partial_x, \partial_y)$ is the horizontal gradient operator, ϕ is the pressure (divided by the uniform density), and τ_s and τ_b are the stresses at the top and bottom of the fluid; τ_s is supplied by the wind. The stress terms have been approximated in a manner consistent with the assumption of z-independent horizontal velocity, $\mathbf{u}(x, y, t)$. The boundary conditions on (2.1–2) are no-normal flow through the bottom,

$$w = -\mathbf{u} \cdot \nabla H \qquad \text{at} \qquad z = -H(x, y), \tag{2.4}$$

and rigid lid,

$$w = 0 \qquad \text{at} \qquad z = 0. \tag{2.5}$$

As in previous papers (Salmon, 1994, and references therein), we prefer to think of the R-term in (2.1) as a Rayleigh friction term. It differs by a fraction $1/H$ from the friction term that would arise from an (unresolved) bottom Ekman layer.

We nondimensionalize (2.1–5) in the usual way, scaling (x, y) by the ocean basin width $L = 4000$ km, z by $H_0 = 4$ km (a representative ocean depth), $\mathbf{u}$ by U, w by UH_0/L, t by L/U, ϕ by f_0UL (where f_0 is a representative value of f), and τ by f_0H_0U. We choose U such that $H_0UL = 30$ Sverdrups, so that a realistic Sverdrup transport corresponds to a nondimensional transport of order unity; this yields $U = 0.2$ km day^{-1}. The nondimensional horizontal momentum equation (2.1) then takes the form,

$$Ro\frac{D\mathbf{u}}{Dt} + y\mathbf{k} \times \mathbf{u} = -\nabla\phi - \epsilon\mathbf{u} + \frac{\tau_s - \tau_b}{H} \tag{2.6}$$

where

$$Ro = \frac{U}{f_0 L} \tag{2.7}$$

is the Rossby number, $\epsilon = R/f_0$, and y is the (nondimensional) Coriolis parameter. Using the numbers given above, $Ro = 0.08 \times 10^{-4}$. Of course, the smallness of Ro conveys a misleading impression of the importance of the inertia terms in (2.6), because the inertia is most important in boundary currents with horizontal scales much less than the basin scale L.

By the continuity equation (2.3) and boundary conditions (2.4–5),

$$H\mathbf{u} = (-\psi_y, \psi_x), \tag{2.8}$$

where ψ is the stream function for the vertically-integrated horizontal transport. Then straightforward manipulations yield the vorticity equation,

$$Ro\frac{\partial \zeta}{\partial t} + J\left(\psi, \frac{Ro\zeta + y}{H}\right) = -\epsilon\zeta + W(x, y), \tag{2.9}$$

where

$$\zeta = \nabla \cdot \left(\frac{1}{H}\nabla\psi\right), \tag{2.10}$$

is the relative vorticity, $J(a, b) \equiv a_x b_y - a_y b_x$ is the horizontal Jacobian, and

$$W(x, y) = \mathbf{k} \cdot \nabla \times \left(\frac{\tau_s - \tau_b}{H}\right). \tag{2.11}$$

We solve (2.9) for $\psi(x, y, t)$, subject to the boundary condition $\psi = 0$ of no transport through the coastline. For given (order-one) wind forcing $W(x, y)$, the two controlling parameters are Ro and ϵ.

In the limit of a flat ocean bottom ($H = 1$), (2.9) reduces to the quasi-geostrophic equation for a single fluid layer of uniform depth. If H is nonuniform, then (2.9) differs from the corresponding quasi-geostrophic equation, but quasi-geostrophic theory applies only to geometries in which the fluid depth varies by a small fraction and thus does not cover the case of primary interest here, in which H vanishes at the coastline.

To solve (2.9), we replace $\partial\psi/\partial t$ by a centered time-difference, and regard the resulting equation as an elliptic equation for ψ at the new time. The only boundary condition is $d\psi/dt = 0$. We treat the (linear) $J(\psi, y/H)$-term semi-implicitly, and use Leonard's (1984) third-order upwind scheme for the (nonlinear) vorticity-advection term in (2.9). The resulting equation is solved by relaxation at each time-step.

The third-order upwinding scheme deserves a few comments. In one dimension (for example), Leonard's scheme replaces the advective operator $u\partial\zeta/\partial x$ by the finite-difference

approximation

$$u\left[\frac{\zeta_{i+1}-\zeta_{i-1}}{2\Delta}-\frac{\zeta_{i+1}-3\zeta_i+3\zeta_{i-1}-\zeta_{i-2}}{6\Delta}\right] \qquad (u>0) \tag{2.12a}$$

where u is positive, and

$$u\left[\frac{\zeta_{i+1}-\zeta_{i-1}}{2\Delta}-\frac{\zeta_{i+2}-3\zeta_{i+1}+3\zeta_i-\zeta_{i-1}}{6\Delta}\right] \qquad (u<0) \tag{2.12b}$$

where u is negative. Here ζ_i is ζ at the i-th gridpoint and Δ is the grid-spacing. It is straightforward to show that

$$(2.12) = u\left(\frac{\partial\zeta}{\partial x}\right)_i + \frac{|u|\Delta^3}{12}\left(\frac{\partial^4\zeta}{\partial x^4}\right)_i + O(\Delta^4). \tag{2.13}$$

Thus the truncation error in (2.13) corresponds to a hyperdiffusion term with a diffusion coefficient proportional to the local fluid speed and to the third power of the grid-spacing. This hyperdiffusion term is responsible for the stability of upwind differencing. (*First*-order upwinding has a truncation error corresponding to *normal* diffusion with a diffusion coefficient of size $u\Delta$, but experience has shown that the diffusion corresponding to first-order upwinding is excessive; see Leonard, 1984.)

In our numerical solution of (2.9), we use a two-dimensional generalization of (2.12) to evaluate the term $\mathbf{u}\cdot\nabla\zeta$ in (2.9). The truncation error corresponds to a hyperdiffusion term $-\kappa\nabla^4\zeta$ on the right-hand side of (2.9), with κ proportional to $|\mathbf{u}|\Delta^3$. Numerical modelers using other advection schemes have often found it necessary to insert such hyperdiffusion terms (sometimes called "high-order eddy viscosities") *explicitly,* to prevent advective straining from producing unresolvable small scales in ζ. In the case of an explicit eddy viscosity, κ is arbitrary but is usually chosen to have the minimum value needed to produce smooth solutions. In the case of third-order upwinding, the flow determines its own (implicit) hyperdiffusion coefficient, but our experience has shown that, even in highly turbulent flow, the hyperdiffusion arising from truncation error is usually sufficient to keep the solution smooth, and that no additional explicit eddy viscosity is needed. None of the solutions described in this paper contains an explicit eddy viscosity.

If an explicit eddy viscosity is used, additional boundary conditions (besides no-normal-flow) must be specified in order to evaluate $\nabla^4\zeta$ near the boundary. It has been demonstrated, however, that solutions of the barotropic vorticity equation are sensitive to the choice of boundary conditions associated with the eddy viscosity (e.g. Cummins, 1992). An advantage of third-order upwinding is that no such additional (and, inevitably, prejudicial) boundary conditions need be specified; since the velocity is tangent to the boundary, the implicit hyperdiffusion acts only *along* the boundary, and thus high-order derivatives normal to the boundary are not required. Recently, third-order upwinding has been shown to provide better results than Laplacian and biharmonic diffusion for

numerically evaluating the advection of a passive tracer in a Stommel gyre in a flat-bottom basin (Hecht *et al.*, 1995).

3. Numerical solutions

We solve (2.9) in a rectangular ocean on $0 < x < 1, 0 < y < 2$ with the southern ($y = 0$) boundary corresponding to the equator. The boundary condition is $\psi = 0$ at the western, northern, and eastern coastlines, and at the equator (where it corresponds to cross-equatorial symmetry of the flow). We consider two cases of topography. In the first case, the ocean bottom is flat ($H = 1$), and all coastal boundaries are vertical walls. In the second case, the ocean depth $H(x)$ vanishes smoothly at the western boundary, with the idealized shelf and slope depicted in Figure 1a, b; the northern and eastern boundaries remain vertical.

To set the stage for our discussion of the effect of topography on inertial western boundary currents, we first briefly consider the solutions of (2.9) in the (linear) limit of no inertia. When $Ro = 0$, the solutions of (2.9) approach the steady state determined by

$$J\left(\frac{y}{H}, \psi\right) = \epsilon \nabla \cdot \left(\frac{1}{H} \nabla \psi\right) - W \tag{3.1}$$

and the boundary condition $\psi = 0$. Following Welander (1968), we regard (3.1) as an advection-diffusion equation for ψ with "stream function" y/H and "source" $-W(x, y)$. According to (3.1), ψ is advected pseudo-westward from the eastern boundary along "streamlines" of constant y/H. In the flat-bottom case, these "streamlines" are latitude lines, and the corresponding "flow" crosses the western boundary at $x = 0$, requiring an ϵ-thickness boundary layer to satisfy the boundary condition $\psi = 0$ there. In the case of the western continental slope of Figure 1a, b, the "streamlines" are the lines of constant y/H shown in Figure 1c. In this case, ψ is advected toward the western equatorial point at which the "streamlines" converge. In the limit $\epsilon \to 0$, friction is important only near this point.

To reiterate, in both the flat-bottom ocean and the ocean with the western shelf, friction is important where the y/H contours intersect the western boundary. The differences in the y/H contours lead to very different boundary current structures: in the flat-bottom basin, the boundary current is a frictional boundary layer at the western vertical side-wall whereas in the basin with the western shelf, the boundary current follows the y/H contours and the effects of the Rayleigh friction are localized in the southwest corner of the basin. It also is worthwhile to remark that in an ocean with closed y/H contours (as when a continental slope is present at all boundaries), the solutions of (3.1) differ from those considered here. In that case, ψ is advected around the closed y/H contours and friction acts to diffuse ψ across these closed contours. These types of solutions have been studied elsewhere (e.g. Rhines and Young, 1983) and are not the focus of the present study.

Figure 2a, b shows the stream function and vorticity in a flat-bottom solution of (3.1). Figure 2c, d shows the corresponding fields in the ocean with the topography of Figure 1a, b. In both cases, $\epsilon = 0.01$. The wind-forcing is nonzero only in the half-basin centered on

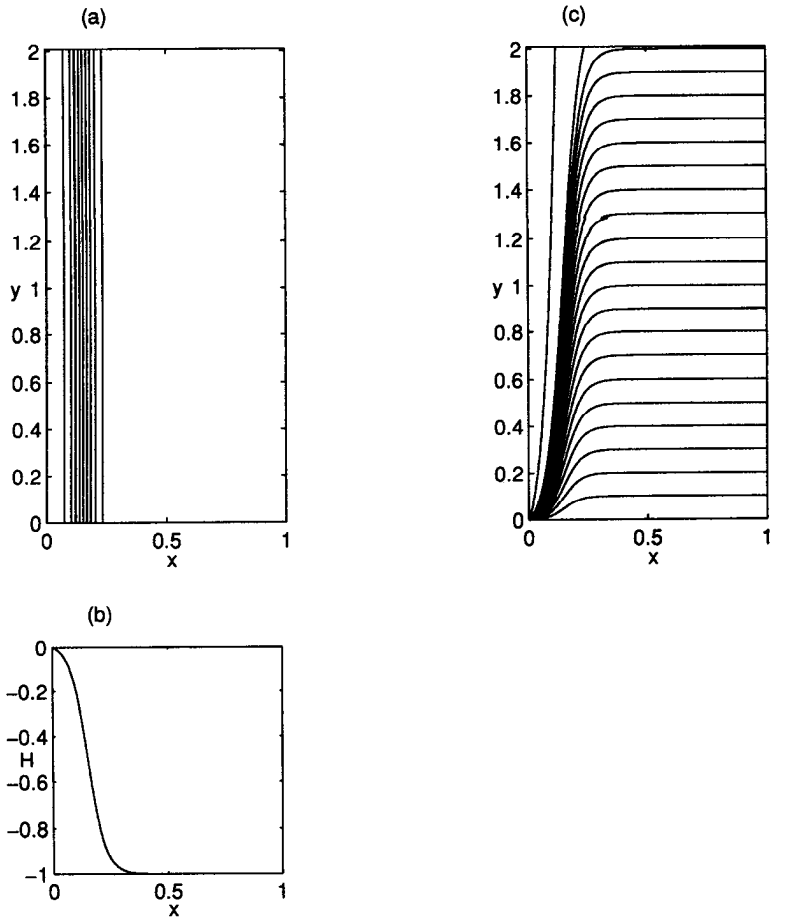

Figure 1. (a, b) The ocean depth $H(x, y)$, which varies from zero at the western coast to 1 in the interior. (c) The corresponding contours of y/H. The continental shelf extends over ¼ of the computational basin (see footnote 3).

the midlatitude, where it is given by

$$W(x, y) = -\sin(2\pi(y - \tfrac{1}{2})) \qquad (\tfrac{1}{2} < y < \tfrac{3}{2}), \tag{3.2}$$

corresponding to subtropical and subpolar gyres antisymmetric about $y = 1$. On $y > \frac{3}{2}$ and $y < \frac{1}{2}$, W vanishes (to remove the effects of the northern and southern boundaries on the inertial solutions considered later). Thus W corresponds to an x-independent "source" of ψ on $\frac{1}{2} < y < 1$, and a "sink" on $1 < y < \frac{3}{2}$.

The flat-bottom solution of Figure 2a, b is essentially that of Stommel (1948), with ϵ near the minimum value needed to resolve the ϵ-thickness boundary layer on the 100 × 200 computational grid. The continental-slope solution of Figure 2c, d has no boundary

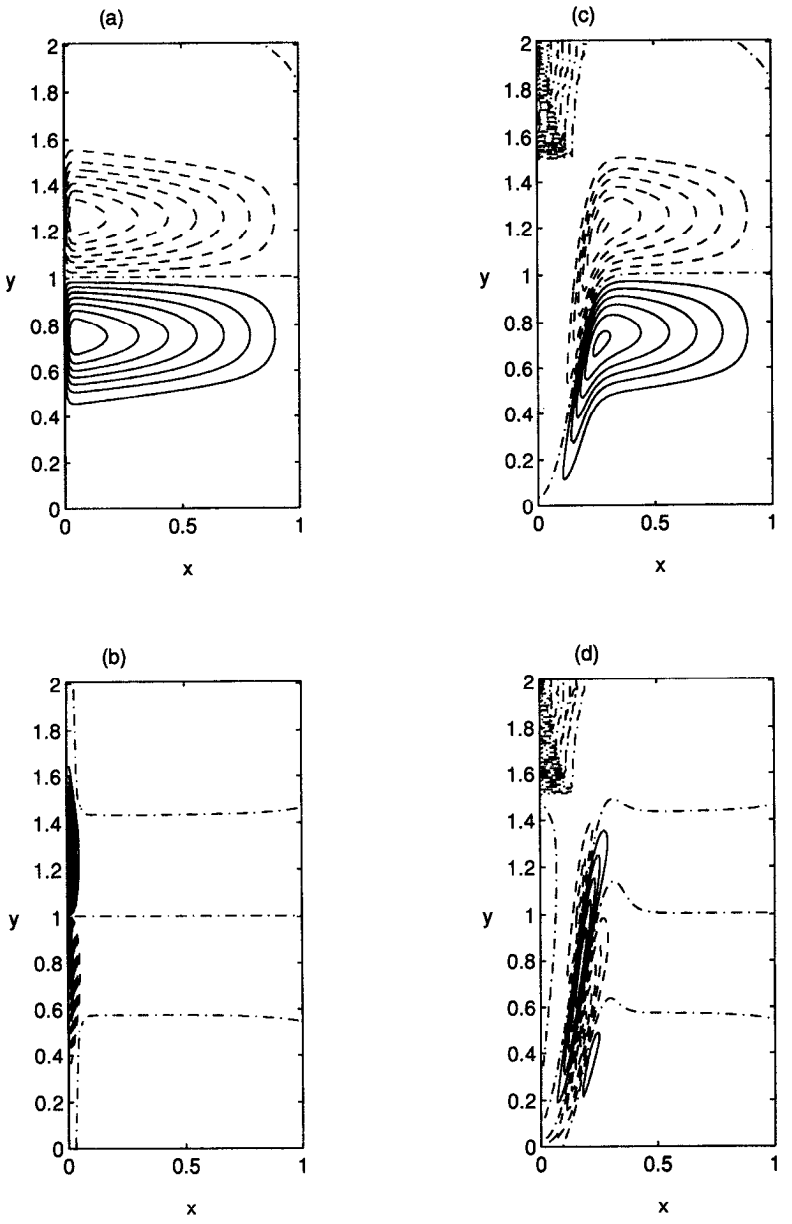

Figure 2. A steady, linear circulation. The transport stream function, ψ, (upper panels) and vorticity multiplied by the ocean depth, $H\zeta$, (lower panels) that satisfy (2.9–10) with $(Ro, \epsilon) = (0.0, 0.01)$, the wind forcing given by (3.2) and (a, b) a flat-bottom basin with $H(x, y) = 1$, and (c, d) a basin with a western shelf, the $H(x, y)$ of Figure 1a, b. The vortex sheets are symmetric and lie in the frictional boundary layer in the flat-bottom solution (b). In the continental-slope solution (d), however, the vortex sheets that correspond to the current shear at the edges of the Gulf Stream are asymmetric and nearly parallel. In all contour plots, the solid/dashed/dot-dash contours correspond to positive/negative/zero values and the contour intervals for ψ and $H\zeta$ are 0.1 and 100, respectively unless indicated. We present contours of $H\zeta$ rather that ζ because of the large values of vorticity that occur in the southwest corner of the basin in the continental-slope solutions.

layer and cannot easily be described analytically, but it is easy to understand on the basis of the analogy between (3.1) and an advection-diffusion equation. Note how the topography breaks the symmetry of the flow about $y = 1$.

In both linear solutions, the vorticity is confined to relatively narrow sheets near the western boundary, but the vortex sheets have a completely different orientation in the two cases, and this has important consequences in what follows. In the flat-bottom solution of Figure 2a, b, the vortex sheets lie within the frictional boundary layer (Fig. 2b) and are well separated from one another. However, in the continental-slope solution of Figure 2c, d, the vortex sheets (whose width is determined by the topography and is independent of the friction) form nearly parallel lines in the southern half-basin. In contrast to Figure 2b, the two vortex sheets in Figure 2d have unequal strengths: the most easterly (negative) vortex sheet (corresponding to the current shear at the seaward edge of the Gulf Stream) is stronger than the (positive) vortex sheet to the west, because of "flow" along y/H-lines into the western sheet has experienced both signs of "source," $-W$.

Now we examine some solutions of (2.9) with nonzero Ro.[3] For sufficiently small Ro, the solutions are steady. Figure 3a, b shows the (steady) stream function and vorticity in the flat-bottom ocean with $Ro = 2.0 \times 10^{-4}$ and $\epsilon = 0.01$. Figure 3c, d shows the (steady) solution in the ocean with continental slope, at the same Ro and ϵ. This value of Ro is near the maximum at which both solutions remain steady. The friction is the same as in the linear solutions of Figure 2. Figure 3a, b which resembles results reported elsewhere in the literature on flat-bottom circulation, shows that the principal effect of inertia on the flat-bottom solutions is the advection of the vortex sheets by the converging western boundary currents. The flow carries the vortex sheets offshore at midbasin, and at this low value of Ro, the flow is essentially symmetric about $y = 1$. The continental-slope solution of Figure 3c, d is more complex, and can perhaps best be understood by regarding the two nearly parallel vortex sheets as parallel rows of oppositely signed point vortices, and considering the motion of each row induced by the other. The stronger, more easterly sheet corresponds to a row of negative vortices, and the vortex sheet to its west corresponds to a somewhat weaker row of positive vortices. Each row induces a northward motion in the other, explaining the slight northward displacement of the western boundary currents from their locations in Figure 2c, d. At the northern tip of the vortex sheets (where the Gulf Stream leaves the coast), the stronger sheet wraps the weaker northern sheet around its tip.

At higher values of Ro, the continental-slope solutions become unsteady. The onset of unsteadiness seems to correspond to the formation of closed contours of the potential vorticity,

$$Q \equiv \frac{Ro\zeta + y}{H}. \tag{3.3}$$

3. In nearly every case, we choose Ro to be somewhat larger than the value given in Section 2, but our larger values are reasonable if one regards our computational basin as the western tenth of an ocean basin with realistic width. In that case, our shelf widths are also not unreasonably wide.

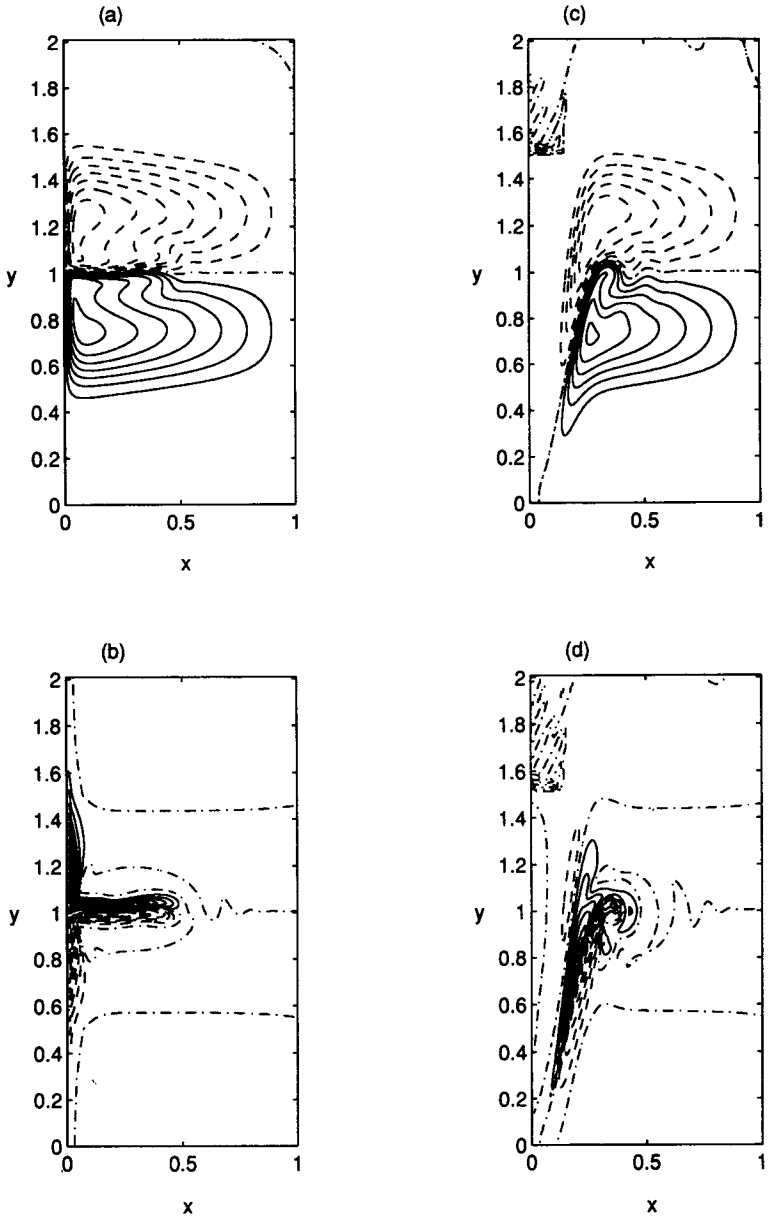

Figure 3. A steady, nonlinear circulation. The same as Figure 2, but with $(Ro, \epsilon) = (2.0 \times 10^{-4}, 0.01)$. In the flat-bottom solution (b), the vortex sheets are advected by the converging western boundary currents. In the continental-slope solution (d), the stronger negative vortex sheet has wrapped the weaker positive sheet around its tip.

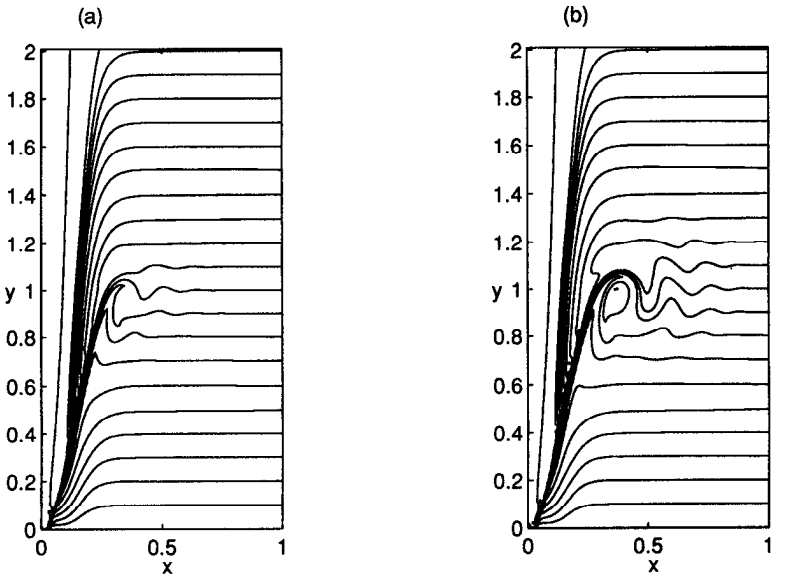

Figure 4. The potential vorticity Q, (3.3), for (a) the steady continental-slope solution of Figure 3c, d and (b) the corresponding continental-slope solution with $(Ro, \epsilon) = (4.0 \times 10^{-4}, 0.01)$ near the onset of unsteadiness when closed contours of potential vorticity appear.

Figure 4a shows the potential vorticity contours in the steady solution of Figure 3c, d ($Ro = 2.0 \times 10^{-4}$) and Figure 4b shows those near the onset of unsteadiness ($Ro = 4.0 \times 10^{-4}$) at which the "overturning" anticipated by Figure 4a is realized and closed contours of Q appear.

For the unsteady solutions, the (entirely kinetic) energy,

$$E = \frac{1}{2}\int\int dxdy \frac{1}{H}\nabla\psi \cdot \nabla\psi, \tag{3.4}$$

is a useful diagnostic. Figure 5a shows time series of the energy (3.4) in continental-slope solutions with $\epsilon = 0.01$ and Ro from 2.0×10^{-4} to 12.0×10^{-4} in increments of 2.0×10^{-4}. A spectral analysis of these time series shows a dominant peak at a frequency of 3.21 ± 0.12 near the onset of unsteadiness at $Ro = 4.0 \times 10^{-4}$. For larger Ro, the dominant spectral peak occurs at a lower frequency and the harmonic content of the spectra increases. The product of the peak frequency and the Rossby number, however, is approximately constant for the solutions shown in Figure 5a.

The unsteadiness in the continental-slope solutions corresponds to eddy formation, where the positive vorticity from the weaker vortex sheet wraps around the closed Q-contour and pinches off, forming a cyclonic eddy. This eddy formation occurs periodically and Figure 6 shows some snapshots of this process at five times during one energy cycle in a solution with $Ro = 8.0 \times 10^{-4}$. At even higher Ro, negative vorticity also

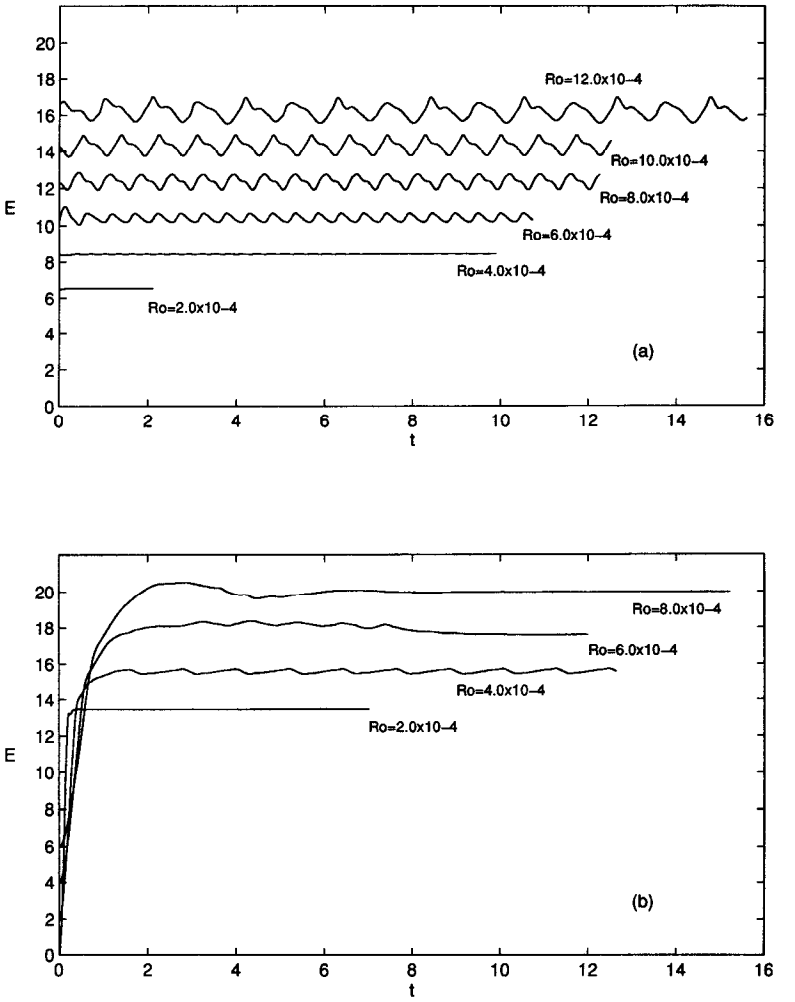

Figure 5. Time series of the energy E, (3.4), for the solutions of (2.9–10) with $\epsilon = 0.01$, the wind forcing (3.2), and (a) $H(x, y)$ of Figure 1a, b and (b) $H(x, y) = 1$. The values of Ro are indicated. The unsteadiness of the continental-slope solutions corresponds to eddy formation while the analogous flat-bottom solutions are steady or quasi-steady, and do not exhibit eddy formation. The energy time series have been offset vertically by an arbitrary amount for clarity.

pinches off, forming anticyclonic eddies in the subpolar gyre. Related numerical results can be found in Becker (1995). The eddy generation presented here is more regular than that in Becker (1995) because the topography and forcing are here symmetric about $y = 1$, and the extent of the wind forcing has been reduced. (In Becker (1995), shelves are located along western and northern coastlines and the wind forcing is over the upper $\frac{2}{3}$ of the basin.)

We next describe the corresponding results in a flat-bottom ocean. As discussed in the introduction, Ierley and Sheremet (1995) and Cessi and Ierley (1995) have shown that

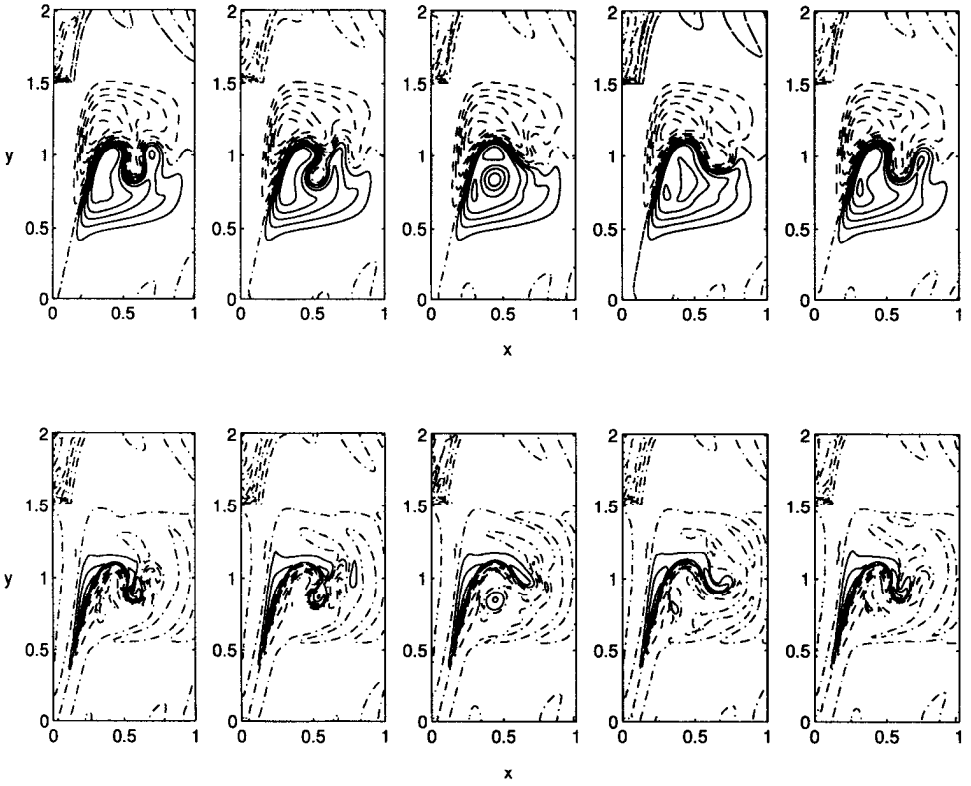

Figure 6. Eddy formation in the basin with the continental shelf. Snapshots of ψ (upper panels) and $H\zeta$ (lower panels) that satisfy (2.9–10) for $(Ro, \epsilon) = (8.0 \times 10^{-4}, 0.01)$, the wind forcing (3.2) and $H(x, y)$ of Figure 1a, b. Time increases from left to right with the left-most snapshot at a time just after an energy maximum and the right-most snapshot at a time just before the next maximum.

flat-bottom dynamics with lateral diffusion have multiple steady solutions for a given set of controlling parameters. In particular, asymmetric, steady circulations may be realized even for symmetric dynamics and antisymmetric forcing (i.e. flat-bottom dynamics with an antisymmetric two-gyre wind). Which circulation is realized depends upon the initial conditions and the stability of the steady circulations. Here, our purpose for considering the flat-bottom solution is to compare with the continental-slope solution rather than to attempt to determine stable attractors of the dynamics (the present dynamics differ from Cessi and Ierley (1995), as we do not consider explicit lateral diffusion and they did not use Rayleigh friction). In this spirit, we conducted a corresponding series of flat bottom experiments for fixed Rayleigh friction, $\epsilon = 0.01$, and increasing Rossby number usually beginning from the initial conditions of rest.

As mentioned above, for small enough Rossby number, the circulation is steady ($Ro = 2.0 \times 10^{-4}$, Figure 3a, b). Figure 5b shows the effect of increasing the Rossby number on the energy time series in the flat-bottom solutions starting from rest. Comparing

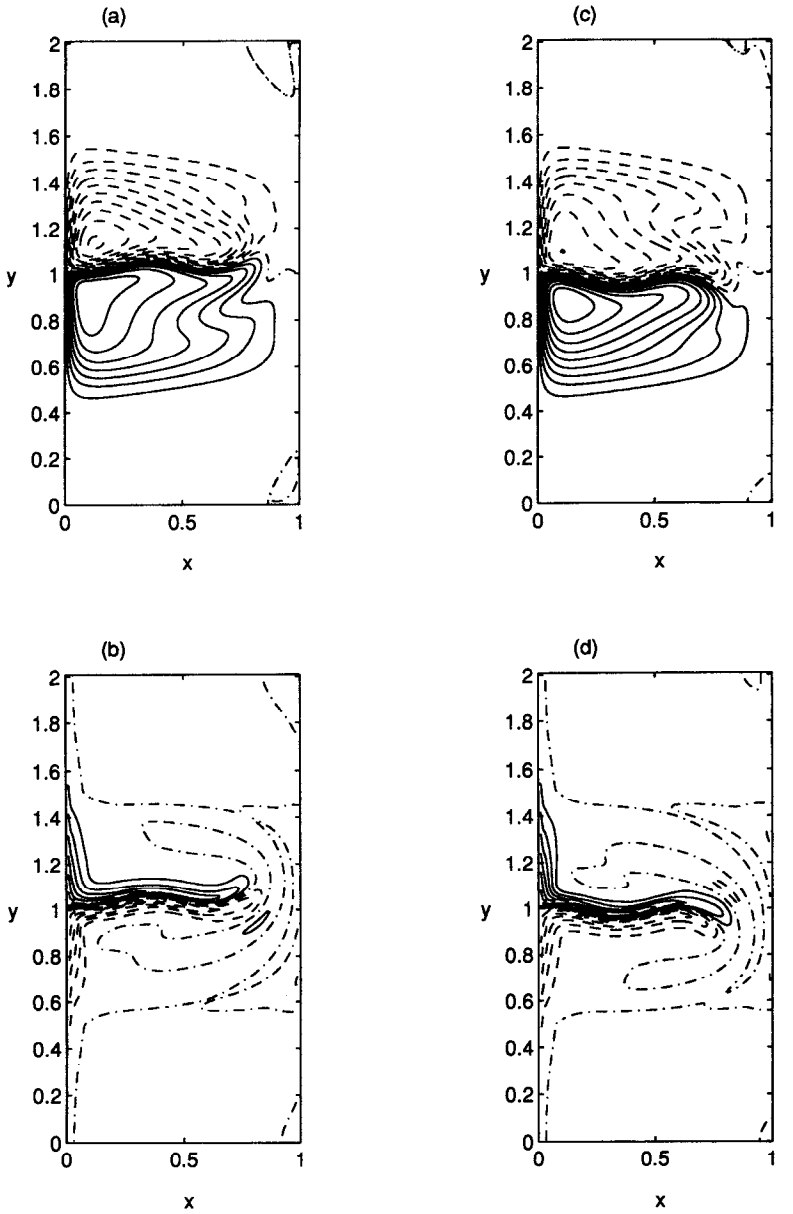

Figure 7. Multiple asymmetric equilibria in a flat-bottom ocean. ψ (upper panels) and ζ (lower panels) that satisfy (2.9–10) for $(Ro, \epsilon) = (6.0 \times 10^{-4}, 0.01)$, the wind forcing of (3.2), and $H(x, y) = 1$. The solution in (a, b) was obtained starting from rest while the solution in (c, d) was obtained starting from a nonzero initial condition.

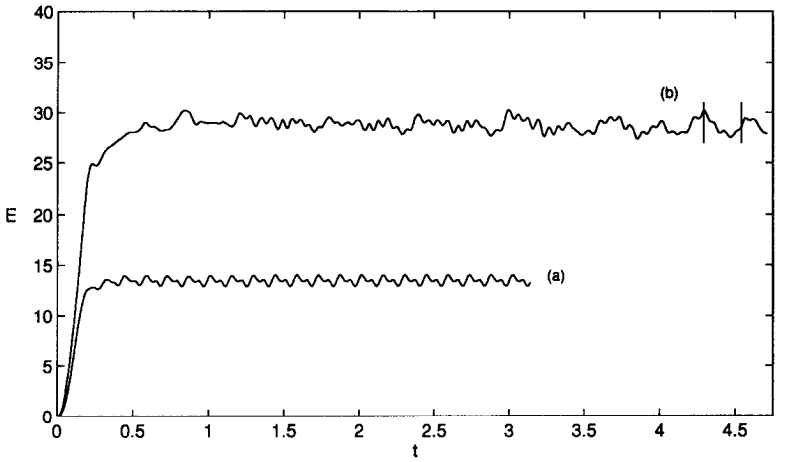

Figure 8. Time series of the energy E, (3.4), for the solutions of (2.9–10) with $(Ro, \epsilon) = (2.0 \times 10^{-4}, 0.005)$, the wind forcing (3.2), and (a) $H(x, y)$ of Figure 1a, b and (b) $H(x, y) = 1$. The hash marks in (b) delimit the start and end times of the snapshots of flat-bottom eddy formation in Figure 11.

with Figure 5a, we see that the energy of the circulation is lower in the basin with the shelf than in the flat-bottom basin because the topography breaks the symmetry of the circulation, and the antisymmetric forcing is more efficient driving the zonal (flat-bottom) flows. Rhines and Schopp (1991) have observed that symmetry breaking due to tilting the wind in a flat-bottom ocean leads to a similar decrease in the energy of the circulation in a three-layer, quasi-geostrophic model.

In addition, Figure 5b shows that with the exception of $Ro = 4.0 \times 10^{-4}$, the flat-bottom solutions starting from rest become steady. The solution for $Ro = 4.0 \times 10^{-4}$ has the vortex sheets carried offshore to about 80% of the basin width and the weak time dependence corresponds to oscillations about an asymmetric (stronger subpolar than subtropical) state, but no eddies form. By varying the initial conditions, another unsteady solution for $Ro = 4.0 \times 10^{-4}$ was obtained that fluctuates about the antisymmetric state, but again no eddies form. For $Ro = 6.0 \times 10^{-4}$, a steady, asymmetric solution was obtained for the initial conditions of rest (Fig. 7a, b). By varying the initial conditions, another asymmetric solution that follows from the symmetry of the flat-bottom dynamics was obtained (Fig. 7c, d). This pair of stable steady solutions appears to be related to those discovered by Cessi and Ierley (1995). For $Ro = 8.0 \times 10^{-4}$, the eastern boundary appears to affect the circulation. While a pair of steady, asymmetric solutions similar to those of Figure 7 was obtained for $Ro = 8.0 \times 10^{-4}$, it also was possible to find a solution for which eddies formed near the eastern boundary, presumably because the jet has reached the eastern boundary.

In all of the foregoing solutions, the Rayleigh-friction parameter had the value $\epsilon = 0.01$. Now we examine some solutions with the lower value of $\epsilon = 0.005$. This value is below that required to resolve an ϵ-thickness boundary layer on our 100×200 grid in the linear

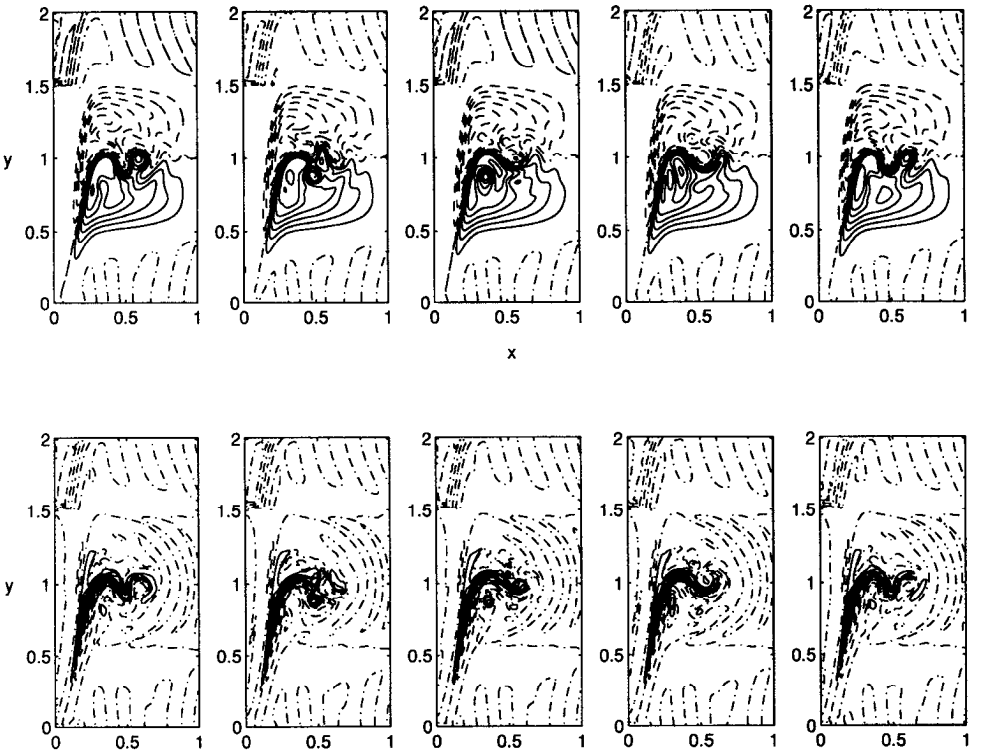

Figure 9. Eddy formation in the basin with the continental shelf. The same as Figure 6, but with $(Ro, \epsilon) = (2.0 \times 10^{-4}, 0.005)$. The diameter of the eddy is smaller here than in the higher Rossby-number, Rayleigh-friction solution of Figure 6. The contour intervals for ψ and $H\zeta$ are 0.1 and 200, respectively.

($Ro = 0$) solutions with a flat bottom. Thus our linear, flat-bottom solutions with $\epsilon = 0.005$ evidently rely on the implicit biharmonic diffusion arising from third-order upwinding.

In the ocean basin with the western continental shelf and $\epsilon = 0.005$, we obtain steady solutions for $Ro = 0.08 \times 10^{-4}$, 0.4×10^{-4}, and 0.8×10^{-4}, while eddy formation is observed for $Ro = 1.0 \times 10^{-4}$, 2.0×10^{-4}, and 4.0×10^{-4}. The latter Rossby number marked the onset of unsteadiness in the higher-frictional case ($\epsilon = 0.01$). A spectral analysis of the energy time series (not shown) shows a dominant spectral peak at a frequency of 11.26 ± 0.47 for $Ro = 1.0 \times 10^{-4}$ near the onset of unsteadiness. As for the $\epsilon = 0.01$ runs in Figure 5a, the dominant spectral peak occurs at a lower frequency for larger Ro, and the product of the peak frequency and the Rossby number is approximately constant.

The energy time series for $(Ro, \epsilon) = (2.0 \times 10^{-4}, 0.005)$ is presented in Figure 8a and resembles that for $(Ro, \epsilon) = (8.0 \times 10^{-4}, 0.01)$ in Figure 5a. In Figure 9, we present snapshots of the $(Ro, \epsilon) = (2.0 \times 10^{-4}, 0.005)$ solution at times in the energy cycle that

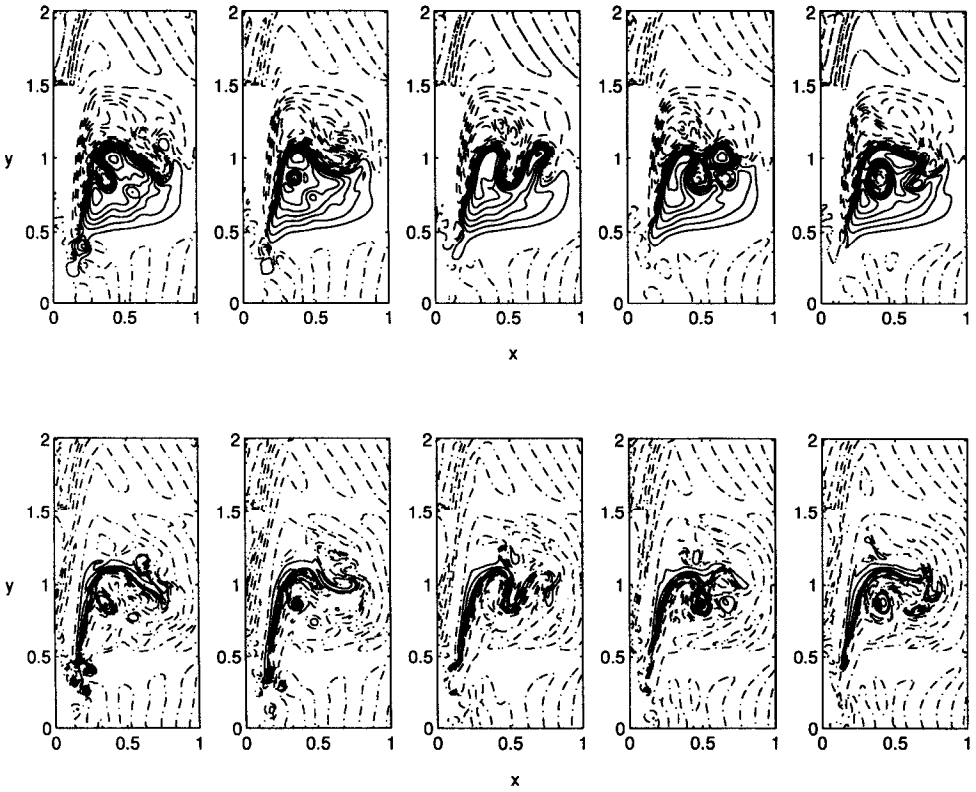

Figure 10. Snapshots of ψ (upper panels) and $H\zeta$ (lower panels) that satisfy (2.9–10) for $(Ro, \epsilon) = (4.0 \times 10^{-4}, 0.005)$, the wind forcing (3.2) and $H(x, y)$ of Figure 1a, b. Time increases from left to right with the left-most snapshot at a time when the third-order upwinding is damping small-scale eddies and the subsequent snapshots are during a period of larger scale eddy formation. Comparing Figures 9 and 10 shows how the eddy diameter increases with Rossby number at a fixed value of the Rayleigh friction. The contour intervals for ψ and $H\zeta$ are 0.1 and 200, respectively.

approximately correspond to those snapshots in Figure 6. Comparing Figures 6 and 9, we conclude that the eddy diameter increases with increasing Rossby number and Rayleigh friction. At $(Ro, \epsilon) = (4.0 \times 10^{-4}, 0.005)$, the energy time series is noisier than any obtained for $\epsilon = 0.01$, and snapshots of this circulation appear in Figure 10. The left-most panel of Figure 10 shows small-scale instabilities at the southern tip of the vortex sheets. Subsequently, the implicit eddy viscosity has damped them out. Comparing Figures 9 and 10 reveals that the eddy diameters increase with Ro at fixed ϵ.

We also computed a few solutions for the flat-bottom ocean at the new, lower value of $\epsilon = 0.005$. At $Ro = 0.08 \times 10^{-4}$, the solution is steady, and by $Ro = 0.8 \times 10^{-4}$, the solution has become weakly unsteady but with no eddy shedding. In contrast to the $\epsilon = 0.01$ solutions, however, eddies begin to form at higher Ro before the jet reaches the eastern boundary. Figure 8b shows the energy time series for a flat bottom solution with $(Ro, \epsilon) =$

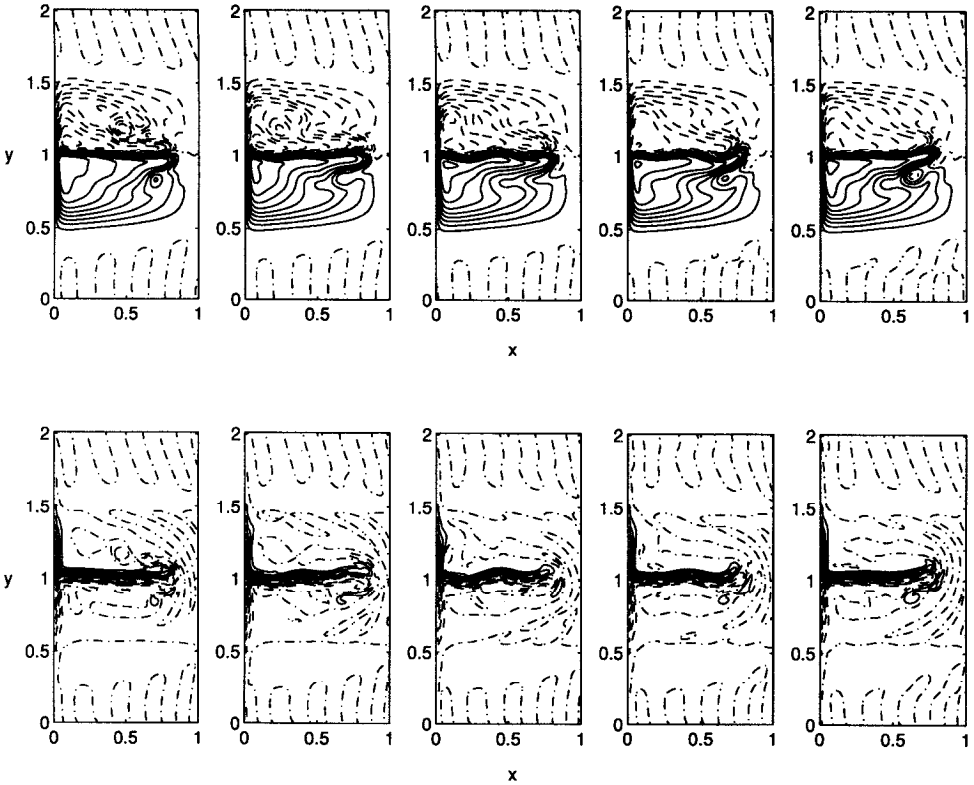

Figure 11. Eddy formation in a flat-bottom basin. Snapshots of ψ (upper panels) and $H\zeta$ (lower panels) that satisfy (2.9–10) for $(Ro, \epsilon) = (2.0 \times 10^{-4}, 0.005)$, the wind forcing (3.2) and $H(x, y) = 1$. Time increases from left to right with the snapshots taken at approximately equally spaced intervals between $t = 4.29$ and 4.54 (see hash marks in Fig. 8b). In contrast to the continental-slope solutions of Figures 9 and 10, eddies form far offshore at the eastern edge of the jet. The contour intervals for ψ and $H\zeta$ are 0.1 and 200, respectively.

$(2.0 \times 10^{-4}, 0.005)$ which is less regular than the corresponding continental-slope solution (Fig. 8a). In Figure 11, we present snapshots of this flat-bottom solution between the times delimited by the hash marks in Figure 8b. It shows that, as has been observed by others in a flat-bottom ocean, the eddies form at the eastern end of the jet (e.g., Rhines and Schopp, 1991).

All the foregoing solutions were computed on a 100×200 grid. To test the sensitivity of our results to the grid-resolution, we also computed some continental-slope solutions on a 50×100 grid. With the lower resolution, we obtain a sequence of unsteady solutions analogous to that of Figure 5a, but at slightly larger Ro. We speculate that the differences between the 50×100 resolution and the 100×200 resolution are due to the dependence of the third-order upwinding on the grid resolution.

Acknowledgments. JMB has been supported by an NSF Mathematical Sciences Postdoctoral Research Fellowship, and a URC Seed Money Award from the University of Hawaii. RS is supported by NSF (Grant no. OCE95-21004). This is SOEST contribution no. 4368.

REFERENCES

Becker, J. M. 1995. An inertial model of the general circulation in an ocean with bottom topography, *in* Proceedings 'Aha Huliko'A Hawaiian Winter Workshop, D. Henderson and P. Müller, eds., 125–130.

Bryan, K. 1963. A numerical investigation of a nonlinear model of a wind-driven ocean. J. Atmos. Sci., *20,* 594–606.

Cessi, P. and G. R. Ierley. 1995. Symmetry-breaking multiple equilibria in quasi-geostrophic wind-driven flows. J. Phys. Oceanogr., *25,* 1196–1205.

Cummins, P. F. 1992. Inertial gyres in decaying and forced geostrophic turbulence. J. Mar. Res., *50,* 545–566.

Fofonoff, N. P. 1954. Steady flow in a frictionless homogeneous ocean. J. Mar. Res., *13,* 254–262.

Hecht, M. W., W. R. Holland and P. J. Rasch. 1995. Upwind-weighted advection schemes for ocean tracer transport: An evaluation in a passive tracer context. J. Geophys. Res., *100,* 20,763–20,778.

Hendershott, M. C. 1987. Single layer models of the general circulation, *in* General Circulation of the Ocean, H. D. I. Abarbanel and W. R. Young, eds., Springer-Verlag, 202–267.

Holland, W. R. 1967. On the wind-driven circulation in an ocean with bottom topography. Tellus, *19,* 582–599.

Ierley, G. R. and V. A. Sheremet. 1995. Multiple solutions and advection-dominated flows in the wind-driven circulation. Part I: Slip. J. Mar. Res., *53,* 703–737.

Leonard, B. P. 1984. Third-order upwinding as a rational basis for computational fluid dynamics, *in* Computational Techniques and Applications: CTAC-83, J. Noye and C. Fletcher, eds., Elsevier North-Holland, 106–120.

Meacham, S. P. and P. S. Berloff. 1997. Barotropic, wind-driven circulation in a small basin. J. Mar. Res., *55,* (in press).

Munk, W. H. 1950. On the wind-driven ocean circulation. J. Meteorol., *7,* 79–93.

Nishigaki, H. 1995. Inertial boundary layer with a velocity front: how the bottom slope controls the western boundary current path. J. Phys. Oceanogr., *25,* 216–225.

Rhines, P. B. and R. Schopp. 1991. The wind-driven circulation: quasi-geostrophic simulations and theory for nonsymmetric winds. J. Phys. Oceanogr., *21,* 1438–1469.

Rhines, P. B. and W. R. Young. 1983. How rapidly is a passive scalar mixed within closed streamlines?, J. Fluid Mech., *133,* 133–145.

Salmon, R. 1994. Generalized two-layer models of ocean circulation. J. Mar. Res., *52,* 865–908.

Stommel, H. 1948. The westward intensification of wind-driven ocean currents. Trans. Am. Geophysical Union, *29,* 202–206.

Veronis, G. 1966. Wind-driven ocean circulation—Part 2. Numerical solution of the nonlinear problem. Deep-Sea Res., *13,* 30–55.

Welander, P. 1968. Wind-driven circulation in one- and two-layer oceans of variable depth. Tellus, *20,* 1–16.

Received: *17 July, 1996;* revised: *31 October, 1996.*